Inorganic Chemistry

pubs.acs.org/IC Article

Dielectric Relaxation and Magnetic Structure of A-Site-Ordered Perovskite Oxide Semiconductor $CaCu_3Fe_2Ta_2O_{12}$

Jianming Deng, Feifei Han, Björn Schwarz, Michael Knapp, Helmut Ehrenberg, Weibo Hua, Manuel Hinterstein, Guobao Li,* Yun He, Jie Wang, Yuan Yuan, and Laijun Liu*

Cite This: *Inorg. Chem.* 2021, 60, 6999−7007

Read Online

ACCESS | Metrics & More | Article Recommendations | SI Supporting Information

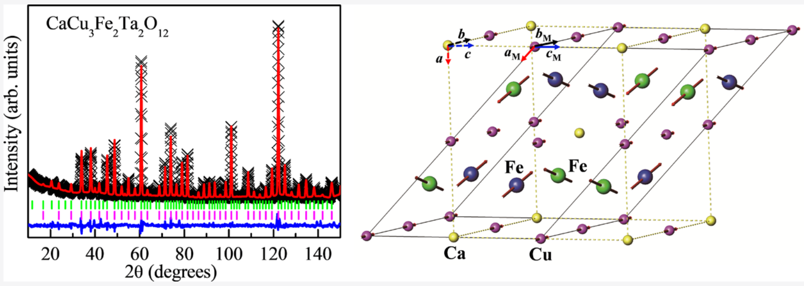

ABSTRACT: A new perovskite oxide semiconductor, $CaCu_3Fe_2Ta_2O_{12}$, was synthesized through a high-pressure and high-temperature approach. The compound possesses an $Im\overline{3}$ space group, where it crystallizes to an A-site-ordered but B-site partial ordered quadruple perovskite structure. Spin ordering occurs around 150 K owing to the antiferromagnetic coupling between Fe^{3+} spins and ferromagnetic coupling between Cu^{2+} spins. The room-temperature dielectric permittivity of $CaCu_3Fe_2Ta_2O_{12}$ was measured to be approximately 2500 at 1 kHz. More importantly, isothermal frequency-dielectric spectroscopy demonstrates the existence of two dielectric relaxations. Debye-like relaxation is attributed to charge carriers trapped among the oxygen vacancies at low temperatures and Maxwell−Wagner polarization relaxation at high temperatures. $CaCu_3Fe_2Ta_2O_{12}$ is a new magnetic semiconductor, where A-site ordering is intercorrelated with second-order Jahn−Teller distortion. These findings offer opportunities to design novel perovskite oxides with attractive magnetic and dielectric properties.

■ INTRODUCTION

Oxides with perovskite or perovskite-related structures are extensively investigated due to the interesting physical properties. Perovskite oxides have the general formula ABO_3, where A site and B site are generally occupied by relatively large-size cations and transition-metal ions, respectively.[1] The structure of ABO_3 consists of the corner-sharing BO_6 octahedral framework where A cations occupy the 12-fold coordinated octahedral interstice. By appropriate substitution for the A site, not only the ordered superstructures are generally stabilized, but also the ordered arrangements of the A cations offer possibilities to design compounds with novel physical properties.

Interesting examples include the A-site-ordered perovskite oxides $AA'_3B_4O_{12}$, where A = alkali, alkaline earth, lanthanide ions; A′ = Cu, Mn; B = Ti, Fe, Cr, Ru, Mn, Co.[2−6] This family of compounds with the perovskite structures presents a particular ordering between the A cations and A′ cations. In particular, the Jahn−Teller Cu^{2+} cation could favor the square-planar site, which rationalizes the unusual modification of $ACu_3B_4O_{12}$ perovskites. A great deal of interesting and unexpected properties has been found for these perovskites, such as giant magnetoresistance in low magnetic fields of $CaCu_3Mn_4O_{12}$,[7] ferromagnetism of $CaCu_3Ge_4O_{12}$ and $CaCu_3Sn_4O_{12}$,[8] heavy-fermion-like behavior of $CaCu_3Ru_4O_{12}$,[9] and charge disproportionation of $CaCu_3Fe_4O_{12}$.[10] Meanwhile, $CaCu_3Ti_4O_{12}$ (CCTO) has received considerable attention, owing to quite high dielectric permittivity ($\varepsilon_r' > 10{,}000$) with very low temperature dependence (above 100 K).[11−14] The microscopic origin of the unusual dielectric behavior of CCTO may be explained in terms of the dielectric relaxation models, such as internal barrier layer capacitors (IBLC) and Maxwell−Wagner (MW) relaxation.[15,16] Based on these dielectric relaxation models, it is easy to get insight into the origin of large dielectric permittivity and dielectric relaxation mechanism. Therefore, the introduction of dielectric relaxation models into the A-site-ordered perovskite oxides offers opportunities for understanding the attractive and unusual dielectric behavior in magnetic materials. In addition, for

Received: October 31, 2020
Published: May 3, 2021

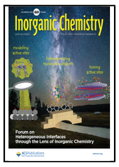

https://doi.org/10.1021/acs.inorgchem.0c03229

$A_2BB'O_6$ double perovskites, B-site cation arrangements play imperative roles in the dielectric properties.[17] Thus, by the introduction of the B-site cations into the A-site-ordered perovskite oxides, the special-ordered arrangements of B-site cations offer possibilities to find new compounds with intriguing dielectric performances. In addition, most A-site-ordered perovskite investigations are restricted in an insulator, and limited work has been reported for oxide semiconductors with magnetic characteristics. The coupling between semiconductors and magnetic semiconductors provides us with multiple degrees of freedom for controlling novel physical properties, and this can be used for optoelectronic devices and energy applications. However, the challenge is that the compounds cannot be prepared in an atmospheric environment. Here, based on a successfully synthesized A-site-ordered oxide semiconductor $CaCu_3Fe_2Ta_2O_{12}$ through a high-pressure combined with high-temperature approach, we investigated its crystal structure and dielectric and magnetic performances. More importantly, we propose two relaxation models to fully understand the unusual dielectric behavior of the magnetic compound.

■ EXPERIMENTAL SECTION

Sample Preparation. A polycrystalline compound of quadruple perovskite $CaCu_3Fe_2Ta_2O_{12}$ was obtained through a high-pressure and high-temperature approach using a hexahedron anvil press (Guilin Guiye Machinery Co., Ltd.). The crystal structure of $CaCu_3Fe_2Ta_2O_{12}$ is A-site-ordered and B-site partial ordered (Figure 1a). The ionic radius of Fe^{3+} and Ta^{5+} is 0.645 (coordination VI) and 0.64 (coordination VI) angstrom, respectively. The starting materials, dried $CaCO_3$, CuO, Fe_2O_3, and Ta_2O_5, were mixed using stoichiometric proportions and then calcined at 850 °C for 4 h. The products were then finely ground and sealed in a Mo/Nb capsule. High-temperature and high-pressure treatments were performed simultaneously at 7 GPa and 1000 °C for 20 min followed by quenching and decompression processes. The large-size sample with a volume of about 2000 mm^3 was obtained from the Mo/Nb capsule.

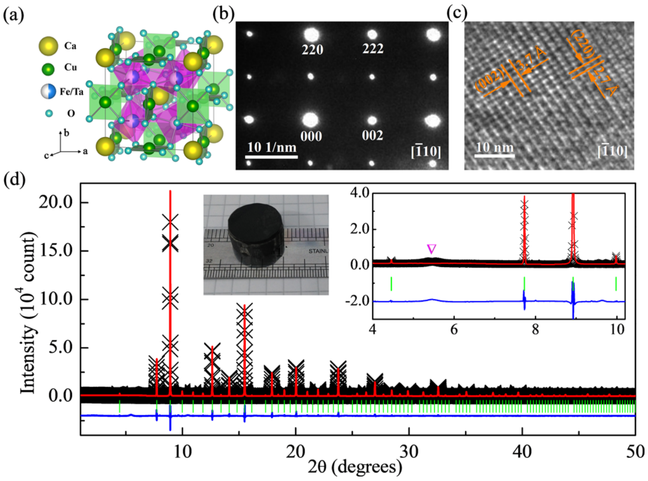

Figure 1. (a) Crystal structure of $CaCu_3Fe_2Ta_2O_{12}$. (b) SAED pattern and (c) corresponding HRTEM image of $CaCu_3Fe_2Ta_2O_{12}$ along the [$\bar{1}$10] zone axis. (d) SXRD pattern and the Rietveld refinement profile of $CaCu_3Fe_2Ta_2O_{12}$. The observed, calculated, and difference patterns and positions of the Bragg reflection are shown by black forks, red line, blue line, and green ticks, respectively. The insets show a large-size specimen placed on a calibrated scale and the diffraction pattern at a low-angle region. The pink nabla symbol indicates impurity in the sample.

Crystal Structure Determination. We carried out crystal structure characterization of $CaCu_3Fe_2Ta_2O_{12}$ by synchrotron X-ray diffraction (SXRD). The strong scattering contrast between Fe and Ta helps us to study the cation ordering degree of the material. In order to minimize absorption, the sample was mounted into 0.5 mm glass capillaries. SXRD data was recorded on a Mythen-1 detector using the ALBA synchrotron with the MSPD beamline[18] of wavelength λ = 0.4134 (20) Å (Cerdanyola del Valles, Spain). Neutron powder diffraction (NPD) patterns were recorded on a SPODI powder diffractometer with a wavelength of 1.548 Å (Garching, Germany).[19] Rietveld refinements of the SXRD and NPD data using the Fullprof software package.[20] High-resolution transmission electron microscopy (HRTEM) and selected area electron diffraction (SAED) were measured using a JEM-2100 (JEOL, Tokyo, Japan).

Physical Measurements. The physical property measurement system (PPMS, Quantum Design) was used to record the magnetic properties of $CaCu_3Fe_2Ta_2O_{12}$. UV-3600 (SHIMADZU, Japan) was used to measure UV−vis diffuse reflectance spectra. The dielectric properties of $CaCu_3Fe_2Ta_2O_{12}$ were performed using a precision impedance analyzer (Agilent 4294A, USA).

■ RESULTS AND DISCUSSION

The global instability index (GII) can be obtained from structural-stability prediction program SPuDS.[21] With GII = 0.036 for $CaCu_3Fe_2Ta_2O_{12}$, this compound was not successfully synthesized under ambient conditions. Therefore, we synthesized the $CaCu_3Fe_2Ta_2O_{12}$ polycrystalline sample through a high-pressure combined with high-temperature method and the photograph of the large-size specimen is shown in the inset of Figure 1d. The SXRD pattern demonstrated the compound to be a cubic perovskite phase with a trace of impurity, as shown in the inset of Figure 1d. Rietveld refinement results for SXRD data and the bond valence sum (BVS) result of $CaCu_3Fe_2Ta_2O_{12}$ are listed in Table 1. Furthermore, the refinement result reveals that the compound possesses an A-site-ordered perovskite structure with the space group $Im\bar{3}$ (no. 204). The atom positions are Ca (0, 0, 0), Cu (0, 1/2, 1/2), Fe/Ta (1/4, 1/4, 1/4), and O (0, *y*, *z*). However, as shown in the inset of Figure 1d, some $h + k + l$ = odd reflections, such as 111 reflection, can not be observed in the SXRD pattern of $CaCu_3Fe_2Ta_2O_{12}$, which associates with the disorder of Fe and Ta cations. The full width at half maximum (FWHM) of the additional peaks are significantly broader than those of fundamental reflections observed at similar 2θ values. The broadening is related to the finite size of the ordered domains.[22] According to the basic Scherrer equation[23] $D = K\lambda/B \cos\theta$, where *B* indicates the additional Lorentz FWHM contribution to $h + k + l$ = odd reflections, the domain size *D* can be well calculated. Furthermore, we also employed HRTEM and SAED to further confirm the structure of $CaCu_3Fe_2Ta_2O_{12}$. As shown in Figure

Table 1. Rietveld Refinement Results for SXRD Data and BVS Result of $CaCu_3Fe_2Ta_2O_{12}$ at 300 K[a]

atom	site	U_{iso} (100×Å^2)	*G*	M−O (Å)	BVS
Ca	2*a*	0.7499(5)	1.0	2.631 (3) × 12	2.04
Cu	6*d*	0.5294(1)	1.0	1.983 (2) × 4	1.95
Fe/Ta	8*c*	0.2640(1)	1.0	2.001 (5) × 6	
O	24*h*	0.5692(1)	0.984		

[a] Space group: $Im\bar{3}$ (no. 204); metal, M; oxygen, O; metal−oxygen bond lengths, M−O; bond valence sum, BVS; residuals R_{wp} = 0.18, R_p = 0.16.

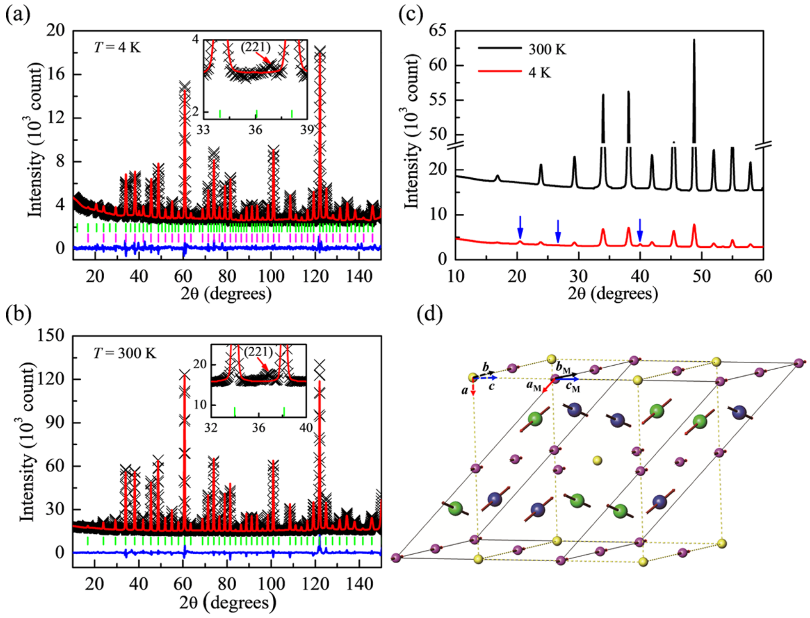

Figure 2. Rietveld plots of NPD data from $CaCu_3Fe_2Ta_2O_{12}$ at (a) 4 K and (b) 300 K. The observed, calculated, and difference patterns are shown by black forks, red line, and blue line, respectively. The first row of ticks in the 4 K refinement corresponds to the nuclear diffractions, while the second one corresponds to the magnetic structure of the sample. The insets of (a) and (b) are a magnified view of the low-angle 221 diffraction peak from the space group $Pn\bar{3}$ due to the Fe and Ta cation partial ordering. (c) Low-angle region of the diffraction patterns at 4 and 300 K. The blue arrows indicate the differences between nuclear and magnetic diffractions. (d) The magnetic structure of $CaCu_3Fe_2Ta_2O_{12}$ at 4 K. The black solid line is the unit cell of magnetic space group $P2$ to describe the magnetic structure, and the yellow dashed line is the unit cell of the space group $Im\bar{3}$ to describe the nuclear structure. For clarity, the yellow balls with no arrows indicate no magnetic Ca^{2+}. The purple balls with red arrows indicate magnetic Cu^{2+}. The blue and green balls with red arrows indicate magnetic Fe^{3+}. The red arrows show the direction of magnetic moment. The dashed line coordinate axis indicates the lattice base vectors (a, b, c), and the solid line one represents the magnetic base vectors (a_M, b_M, c_M).

Table 2. Rietveld Refinement Details of NPD Diffraction Data from $CaCu_3Fe_2Ta_2O_{12}$ at 4 K[a]

atom	site	x	y	z	G	U_{iso} (Å^2)
Ca	2*a*	0.0000	0.0000	0.0000	1.0	0.0109
Cu	6*d*	0.0000	0.5000	0.5000	1.0	0.0081
Fe/Ta	8*c*	0.2500	0.2500	0.2500	1.0	0.0063
O	24*h*	0.0000	0.8238(3)	0.3041(1)	0.984	0.0068

[a] Space group: $Im\bar{3}$ (no. 204); site occupation factors, G; isotropic thermal parameters, U_{iso}; lattice parameter, a = 7.5039(2) Å; residuals R_{wp} = 0.038, R_p = 0.027.

Table 3. Rietveld Refinement Details of NPD Diffraction Data from $CaCu_3Fe_2Ta_2O_{12}$ at 300 K[a]

atom	site	x	y	z	G	U_{iso} (Å^2)
Ca	2*a*	0.0000	0.0000	0.0000	1.0	0.0159
Cu	6*d*	0.0000	0.5000	0.5000	1.0	0.0101
Fe/Ta	8*c*	0.2500	0.2500	0.2500	1.0	0.0082
O	24*h*	0.0000	0.8256(3)	0.3052(3)	0.984	0.0072

[a] Space group: $Im\bar{3}$ (no. 204); lattice parameter a = 7.5154(1) Å; residuals R_{wp} = 0.071, R_p = 0.051.

1b, note that no clear diffraction spots with $h + k + l$ = odd reflections can be observed in the SAED pattern of the sample, such as the 111 spot, indicating that Fe and Ta cations are in a random arrangement at the B-site. For the HRTEM image in Figure 1c, the characteristic spacings of the (002) and (220) lattice planes are 0.37 and 0.27 nm, respectively, which is in agreement with the refined lattice parameters. All of these results are well matched, which confirm that $CaCu_3Fe_2Ta_2O_{12}$ belongs to the cubic structure with the space group $Im\bar{3}$, where only Ca and Cu ordering occurs at the A-site, as shown in Figure 1a.

The compound crystallizes in an $Im\bar{3}$ space group, and the possible space groups in perovskite oxides with the general formula $AA'_3B_2B'_2O_{12}$ are summarized in Table 4. Surprisingly, short Cu−O bond lengths of 1.983(2) Å were found in $CaCu_3Fe_2Ta_2O_{12}$, showing a square-planar coordination of oxygen with distortion at the A′-site. Thus, this results in considerable tilting of the FeO_6 and TaO_6 octahedra. Based on the BVS method,[24] the valence states of A-site cations (Ca and Cu) can be estimated by metal−oxygen bond lengths, but the reliable valence states of B-site cations (Fe and Ta) are not accurately calculated due to the Fe/Ta disorder in $CaCu_3Fe_2Ta_2O_{12}$, as shown in Table 1.

We also analyzed the NPD patterns by the Rietveld method to further confirm the crystal and magnetic structures of $CaCu_3Fe_2Ta_2O_{12}$, as shown in Figure 2. The parameters of the refined structure are listed in Tables 2 and 3. The crystal structure of an $AA'_3B_2B'_2O_{12}$ perovskite was refined through a starting model derived by SPuDs.[25] As shown in Figure 2a,b patterns of 4 and 300 K have no significant difference, indicating that the compound crystallizes in the $Im\overline{3}$ space group. The $h + k + l$ = odd reflection is absent in the NPD patterns, such as the111 reflection. This suggests a disordered arrangement of Fe and Ta cations at the B-site, which is consistent with the results obtained from SXRD and SAED. Nevertheless, a B-site-ordered diffraction peak from the space group $Pn\overline{3}$, such as 221, in NPD was observed, as shown in the insets of Figure 2a,b indicating the random distribution of Fe and Ta cations in most of the regions in $CaCu_3Fe_2Ta_2O_{12}$ and a small account of local B-site ordering regions. The preparation of $CaCu_3Fe_2Ta_2O_{12}$ by a high-pressure synthesis method, in which the quenching process is commonly used, will easily introduce a certain degree of ion disorder into the compound. The average Fe/Ta−O bond length is consistent with that obtained from tabulated ionic radii.[26] Site-occupancy refinements show apparent oxygen off-stoichiometry in $CaCu_3Fe_2Ta_2O_{12}$.

The magnetic structure of $CaCu_3Fe_2Ta_2O_{12}$ is carried out by NPD at 4 K, as shown in Figure 2c. Note that magnetic diffraction peaks are different from the nuclear diffraction peaks in $CaCu_3Fe_2Ta_2O_{12}$, suggesting the presence of a magnetic superstructure. The magnetic structure of $CaCu_3Fe_2Ta_2O_{12}$ is shown in Figure 2d. The dashed line coordinate axis indicates the lattice base vectors (a, b, c), and the solid line one represents magnetic base vectors (a_M, b_M, c_M). The magnetic space group is $P2$ with a = 10.6121 Å, b = 7.5039 Å, c = 7.5039 Å, α = 90.00°, β = 135.00°, and γ = 90.00°. The coordination for Cu^{2+} is (0.0000, 0.0000, 0.5000), (0.5000, 0.5000, 0.5000), (0.0000, 0.5000, 0.5000), (0.5000, 0.0000, 0.5000), (0.0000, 0.5000, 0.0000), and (0.5000, 0.0000, 0.0000). The coordination for Fe^{3+} is (0.2500, 0.7500, 0.5000), (0.75000, 0.2500, 0.0000), (0.2500, 0.2500, 0.5000), and (0.75000, 0.7500, 0.5000). The Cu^{2+} moments are along the b-axis with small ferromagnetic ordered of 1.14 (4) μ_B/fu. The Fe^{3+} moments for the four sites are (−0.679, 2.967, −0.529), (0.679, −2.967, 0.529), (−0.679, 2.967, −0.529), and (0.679, −2.967, 0.529) μ_B/fu. They are antiferromagnetic ordered of 3.09 (4) μ_B/fu, which is very different from that for other A-site-ordered quadruple perovskite systems. Therefore, $CaCu_3Fe_2Ta_2O_{12}$ possesses spin ordering consisting of the antiferromagnetic coupling between Fe^{3+} spins and ferromagnetic coupling between Cu^{2+} spins. The net magnetic moment of $CaCu_3Fe_2Ta_2O_{12}$ is dominated by Cu^{2+} moments.

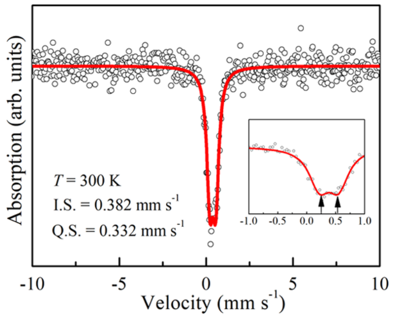

Figure 3. Mössbauer spectrum of $CaCu_3Fe_2Ta_2O_{12}$ at 300 K. The black dots represent the observed spectrum, and the red solid line represents the fitting curve. The inset shows the Mössbauer spectrum near 0 mm s^{-1}.

Figure 3 shows the Mössbauer spectrum of $CaCu_3Fe_2Ta_2O_{12}$ observed at 300 K. The linewidth of the spectrum is much broader, but a typical quadrupole doublet is observed, indicating that the line profile is a typical characteristic of a compound shape. The arrangement of diverse cations around the Fe site can not only give rise to the corresponding arrangement of the electric field gradient tensor but also generate an obvious non-cubic symmetry at the Fe site in the cubic structure identified from X-ray diffraction.[27] Based on a single doublet fitting, the values of the isomer shift (I.S.) and quadrupole splitting (Q.S.) can be obtained, which are found to be 0.382 and 0.332 mm s^{-1}, respectively. The apparent quadrupole splitting was observed, revealing the non-cubic symmetry of the Fe atoms. Similar spectrum were found in double perovskite $SrLaFeSnO_6$,[27] where Sr/La atoms and Fe/Sn atoms are both in a random arrangement at the A-site and B-site, respectively, leading to local electric field gradient at the Fe site. Meanwhile, it gave the same explanation, where local structural distortions in disordered Ca_2FeTaO_6[28] generate the large splitting of the spectrum caused by the significant charge difference between Fe^{3+} and Ta^{5+}. Therefore, Mössbauer spectrum reveals that the $CaCu_3Fe_2Ta_2O_{12}$ perovskite displays a partially ordered arrangement of Fe and Ta cations, and this arrangement is essentially disordered.

From the temperature-dependent magnetic susceptibility data shown in Figure 4a, measured with a 10 kOe external field, a clear paramagnetic state with linear inverse magnetic susceptibility cannot be observed up to 350 K. The inverse magnetic susceptibility significantly decreases with decreasing temperature from the highest temperature down to approximately 150 K, which could associate with the not perfect disorder and the presence of local B-site cation ordering in $CaCu_3Fe_2Ta_2O_{12}$. Below 150 K, spin ordering is indicated and the measured magnetization exhibits smaller values as compared to a pure Curie−Weiss $\sim 1/T$ type behavior of a paramagnetic substance theoretically extrapolated to lower temperatures. There exists nonmagnetic Ta^{5+} ($5d^0$) ion in $CaCu_3Fe_2Ta_2O_{12}$; therefore, observation of low-temperature magnetization is attributed to A′-site Cu^{2+} contributing as S = 1/2 with 1 μ_B and B-site Fe^{3+} as S = 5/2 with 5 μ_B to the ordered moment at low temperatures. Note that the observed magnetization is 0.39 μ_B/fu at 10 kOe and at 5 K without saturation, as presented in Figure 4b. The observed magnetization matches very well that obtained from the net magnetic moment from neutron diffraction. Therefore, the antiferromagnetic coupling between Fe^{3+} spins and ferromagnetic coupling between Cu^{2+} spins give rise to a net magnetic moment as indicated from these measurements to some extent.

The observed value of magnetization is consistent with the B-site-disordered $CaCu_3Fe_2Nb_2O_{12}$ perovskite.[22] The transition temperature (T_N) and magnetic moment in perovskite oxides with the general formula $AA'_3B_2B'_2O_{12}$ are summarized in Table 4. For the double perovskite Sr_2FeTaO_6,[28] the spin-glass transition temperature (25 K) is significantly lower than the magnetic transition temperature of $CaCu_3Fe_2Ta_2O_{12}$ (150 K) due to only the Fe^{3+}−Fe^{3+} interaction in Sr_2FeTaO_6. Meanwhile, the magnetic transition temperature of $CaCu_3Fe_2Ta_2O_{12}$ (150 K) is also higher than for other A-site-ordered perovskites with the magnetic A′-site Cu^{2+} cation. For instance, it is 6 times larger than that of antiferromagnetic $CaCu_3Ti_4O_{12}$ (25 K) and 15 times larger than that of ferromagnetic $CaCu_3Sn_4O_{12}$ (10 K), in which only the A′-site

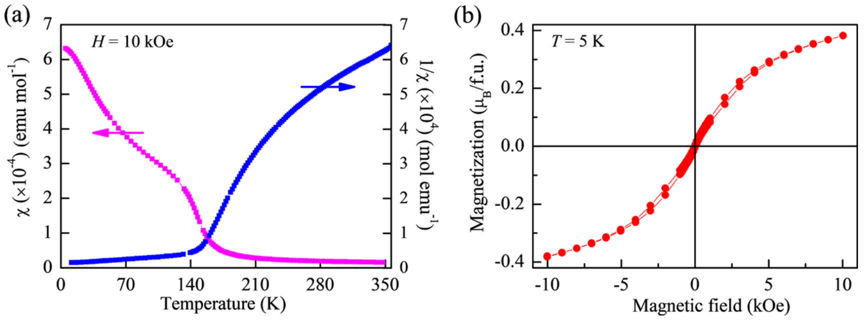

Figure 4. (a) Temperature dependence of magnetic susceptibility and inverse susceptibility measured at 10 kOe of $CaCu_3Fe_2Ta_2O_{12}$. (b) Field dependence of magnetization of $CaCu_3Fe_2Ta_2O_{12}$ at 5 K.

Table 4. Comparison of the Space Group, Transition Temperature (T_N), Magnetic Moment, and Dielectric Permittivity in Perovskite Oxides with the General Formula $AA'_3B_2B'_2O_{12}$

sample	A/B-site ordered	space group	T_N (K)	magnetic moment (μ_B/fu)	dielectric permittivity
$CaCu_3Fe_2Re_2O_{12}$[40]	A- and B-site ordered	$Pn\bar{3}$	560	8.7	
$CaCu_3Fe_2Sb_2O_{12}$[41]	A- and B-site ordered	$Pn\bar{3}$	170	5.7	
$CaCu_3Fe_2Nb_2O_{12}$[22]	A- and B-site ordered	$Pn\bar{3}$	170	5.7	
$CaCu_3Fe_2Nb_2O_{12}$[22]	A-site-ordered	$Im\bar{3}$		0.65	
$CaCu_3Cr_2Sb_2O_{12}$[42]	A- and B-site ordered	$Pn\bar{3}$	160	1.4	
$CaCu_3Cr_2Ru_2O_{12}$[43]	A-site-ordered	$Im\bar{3}$	140	0.05	
$CaCu_3Ga_2Sb_2O_{12}$[44]	A- and B-site ordered	$Pn\bar{3}$			12
$CaCu_3Fe_2Ta_2O_{12}$ (this work)	A-site-ordered	$Im\bar{3}$	150	0.39	25

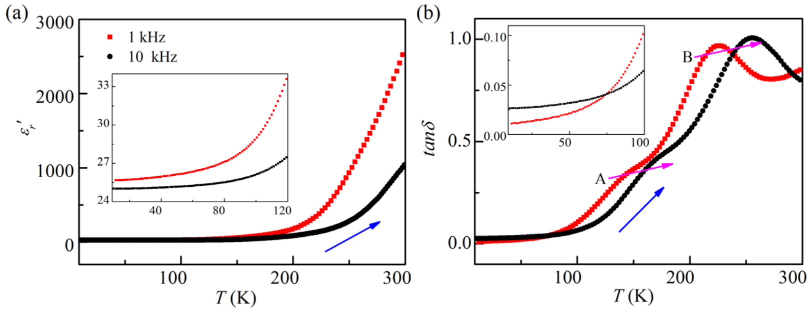

Figure 5. Temperature dependence of (a) dielectric permittivity ε'_r and (b) dielectric loss tan δ of $CaCu_3Fe_2Ta_2O_{12}$ at both 1 and 10 kHz. The insets show an expanded view of the dielectric spectrum at a low-temperature region.

Cu^{2+} ($S = 1/2$) spins contribute to the magnetic behavior.[29,30] Introducing the B-site Fe^{3+} ions in $CaCu_3Fe_2Ta_2O_{12}$ provides an additional $Fe^{3+}(\uparrow)-Fe^{3+}(\downarrow)$ antiferromagnetic coupling as strong as that of the A′-site $Cu^{2+}(\uparrow)-Cu^{2+}(\uparrow)$ ferromagnetic coupling. Therefore, the much stronger $Fe^{3+}(\uparrow)-Fe^{3+}(\downarrow)$ antiferromagnetic and $Cu^{2+}(\uparrow)-Cu^{2+}(\uparrow)$ ferromagnetic exchange energies dominate the weaker $Cu^{2+}-Fe^{3+}$ interaction and lead to $CaCu_3Fe_2Ta_2O_{12}$ with a higher magnetic transition temperature (150 K) relative to that of the B-site nonmagnetic $CaCu_3Ti_4O_{12}$ (25 K) and $CaCu_3Sn_4O_{12}$ (10 K). In contrast, the magnetic transition temperature of $CaCu_3Fe_2Ta_2O_{12}$ (150 K) is much less than that of $LaFeO_3$ (740 K) with $Fe^{3+}-Fe^{3+}$ interaction. As is well known, the magnetic transition temperature is strongly dependent on the B-site and B′-site cation ordering as well as on the superexchange interaction.[31] In $LaFeO_3$, the larger overlap of electron orbitals gives rise to larger superexchange interactions that result in a higher magnetic transition temperature.[32] In the B-site-disordered perovskite $CaCu_3Fe_2Ta_2O_{12}$, the significantly lower magnetic transition temperature is rationalized within the Fe^{3+}/Ta^{5+} vibronic superexchange interaction. Therefore, the B-site-disordered perovskite $CaCu_3Fe_2Ta_2O_{12}$ has a much lower magnetic transition temperature relative to that of $LaFeO_3$.

To further confirm the electronic property of $CaCu_3Fe_2Ta_2O_{12}$, we measured the UV−vis diffuse reflectance spectra in Figures S1a and S1b in the Supporting Information. The experimental result suggests that $CaCu_3Fe_2Ta_2O_{12}$ is a semiconductor and the band gap is approximately 1.77 eV, which is consistent with the theoretical calculation.[33] Figure S1c displays the temperature-dependent resistance and electrical resistivity of the compound. Although $CaCu_3Fe_2Ta_2O_{12}$ has high resistivity at room temperature, the feature is evidently consistent with a semiconducting behavior. Prominent electrical conductivity may be due to the existence of Fe-rich or Ta-rich clusters caused by the Fe/Ta cation disorder at the B-site. As shown in Figure S1d, the electrical conductivity of $CaCu_3Fe_2Ta_2O_{12}$ increases as the temperature increases. The electrical transport can be described as a semiconducting behavior, and the electrical conductivity can be expressed as

$$\sigma = \sigma_0 \exp(E_a/k_B T) \quad (1)$$

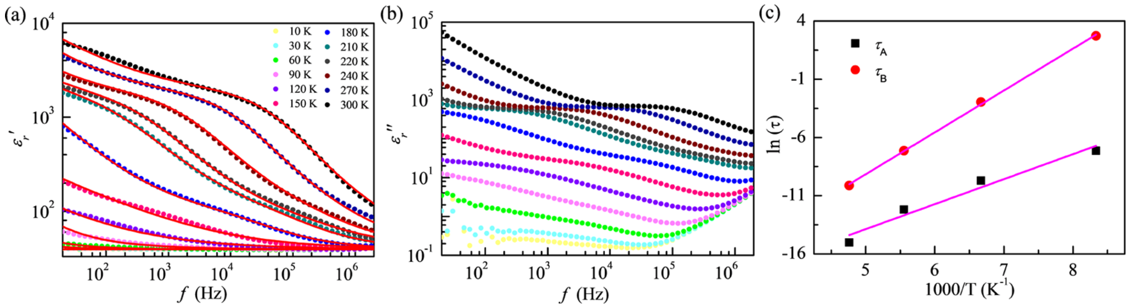

Figure 6. Frequency dependence of (a) ε_r' and (b) ε_r'' of $CaCu_3Fe_2Ta_2O_{12}$. The red solid curves indicate the fitting result based on eq 5 for ε_r'. (c) Temperature dependence of the relaxation time of $CaCu_3Fe_2Ta_2O_{12}$. The data are linearly fitted based on eq 6.

Table 5. Parameters ε_s, ε_∞, α, s, and τ Obtained from Fitting by the Modified Cole−Cole Relaxation of $CaCu_3Fe_2Ta_2O_{12}$ at Selected Temperatures

T (K)	ε_{s1}	ε_{s2}	ε_∞	α_1	α_2	s	τ_1	τ_2
120	1544	93.5	39.5	0.56	0.69	0.70	8.12×10^{-4}	15.13
150	1601	95.5	39.5	0.55	0.59	0.68	6.32×10^{-5}	0.052
180	1635	97.5	39.5	0.42	0.42	0.66	5.92×10^{-6}	8.48×10^{-4}
210	1646	99.5	39.5	0.37	0.39	0.63	3.67×10^{-7}	4.27×10^{-5}

where σ_0, k_B, T, and E_a are the pre-exponential factor, Boltzmann constant, absolute temperature, and conduction activation energy, respectively. The E_a is 0.70 eV by least-squares fit to the entire data. Note that the E_a is approximately half of the band gap.[34] It indicates the thermally activated process of the intrinsic charge carriers.

Figure 5 highlights the temperature dependence of the dielectric properties of $CaCu_3Fe_2Ta_2O_{12}$. The both ε_r' and tan δ of the sample are weakly temperature-dependent over a wide temperature range (below 200 K). The sample shows an intrinsic dielectric permittivity of $\varepsilon_r' \approx 25$ at low temperatures, which is a half of CCTO (intrinsic $\varepsilon_r' \approx 60$).[35−37] Such a low dielectric response is attributed to suppression of cooperative switching in either the local electric polarization or the atomic displacements caused by lattice distortion due to the B-site-disordered arrangement. The intrinsic dielectric permittivity values in perovskite oxides with the general formula $AA'_3B_2B'_2O_{12}$ are summarized in Table 4. At low temperatures, freezing of electric dipoles results in the dramatic decrease in ε_r' value. However, the ε_r' undergoes a step-like increase at a higher temperature due to the thermally activated process of the charge carriers.[38] Moreover, two frequency dependencies of the loss factor are clearly observed between 100 and 300 K, corresponding to two dielectric relaxations marked as A and B, as shown in Figure 5b. Actually, both dielectric relaxations can be attributed to a thermally activated process, which originate from two independent mechanisms: (a) the relaxation A is related to polarons (the charge carriers trapped at the oxygen vacancies).[39] This is expected to give rise to a Debye-like relaxation. Thus, the relaxation A is dominated by a Debye-like relaxation; (b) with further increasing the temperature, the thermally activated charge carriers accumulate on the grain boundaries in the samples that have different conductivities to screen the polarization discontinuity. This extrinsic source of dielectric relaxations is known as the MW relaxation. However, the influence of B-site disorder on the local potential fluctuation leads to a change in MW polarization in $CaCu_3Fe_2Ta_2O_{12}$, which gives rise to the significant enhancement of ε_r' at high temperatures. Therefore, the relaxation B stems from the MW polarization modified by the B-site disorder.

To further study the mechanism of the dielectric response in $CaCu_3Fe_2Ta_2O_{12}$, we performed the frequency dependence of ε_r' and ε_r'' of the dielectric permittivity at selected temperatures. As demonstrated in Figures 66ba and , the ε_r' shows the high values at a low-frequency region, and it significantly decreases as the frequency increases. As the temperature increases, the step-like decrease shifts to a higher frequency, which is accompanied by the movement of ε_r'' peaks, and such a behavior is a clear characteristic of the Debye-like relaxation.[45,46] This is an intrinsic relaxation at high frequencies that originates from charge carriers trapped at the oxygen vacancies (polarons). The partial reduction of Cu^{2+} and Fe^{3+} to Cu^+ and Fe^{2+}, respectively, and traces of oxygen vacancies are created, which is consistent with the refinement result obtained from NPD patterns, as shown in eqs 2−4.

$$O_o \rightleftharpoons \frac{1}{2}O_2(\uparrow) + V_O^{\cdot\cdot} + 2e' \tag{2}$$

$$Cu^{2+} + e' \rightleftharpoons Cu^+ \tag{3}$$

$$Fe^{3+} + e' \rightleftharpoons Fe^{2+} \tag{4}$$

As is well known, the preparation of perovskite oxide ceramics by a high temperature sintering method, such as $SrTiO_3$ and $BaTiO_3$,[47,48] will also easily introduce intrinsic oxygen vacancies into ceramic samples due to traces of reduced Ti at high temperatures. However, the relaxation is not observed owing to the limited measurement window at low frequencies. The prominent increase in ε_r'' at low frequencies is attributed to enhancement of thermally activated conductivity. In many dielectric materials, the conductivity is related to the dielectric relaxation that has been observed at low frequencies.[49] Therefore, it is imperative to establish the relationship between the dielectric relaxation behavior and defect compensation mechanisms based on the dielectric relaxation model for the diffuse dielectric anomaly associated with electrical conduction.

https://doi.org/10.1021/acs.inorgchem.0c03229
Inorg. Chem. 2021, 60, 6999−7007

When the contribution of electrical conduction cannot be neglected in dielectric materials, the term of electrical conduction is generally added to the double Cole−Cole equations, as shown in eq 5.

$$\varepsilon^* = \varepsilon_\infty + \left(\frac{\varepsilon_{s1} - \varepsilon_\infty}{1 + (j\omega\tau)^{1-\alpha_1}}\right) + \left(\frac{\varepsilon_{s2} - \varepsilon_{s1}}{1 + (j\omega\tau)^{1-\alpha_2}}\right) - \frac{j\sigma^*}{\varepsilon_0\omega^s} \tag{5}$$

where ε_{s1} and ε_{s2} are the static dielectric permittivity of the relaxations A and B, respectively, ε_∞, ω, and τ represent the dielectric permittivity at very high frequencies, angular frequency, and relaxation time, respectively, s $(0 < s < 1)$ is a constant, and σ^* represents the complex conductivity. This relationship reveals that the electrical conduction may contribute to $\varepsilon_r'$and ε_r''. The fitting results of $CaCu_3Fe_2Ta_2O_{12}$ are shown in Figure 6a. Simultaneously, we obtain the fitting parameters of ε_{s1}, ε_∞, α, s, and τ as summarized in Table 5. The reduction in α with increasing temperature indicates that the low-temperature relaxation is close to the ideal Debye relaxation. In addition, a rapid decrease in τ with increasing temperature suggests a faster polarization process due to the enhancement in dipole density. To get insight into the two dielectric relaxation behaviors, the dielectric relaxations are described by the Arrhenius law

$$\tau = \tau_0 \exp(E_a/k_B T) \tag{6}$$

where τ represents the relaxation time, τ_0 and k_B are constants, and E_a indicates the activation energy. As shown in Figure 6c, a linear fitting $E_A = 0.185$ eV is for relaxation A and $E_B = 0.310$ eV for relaxation B. The activation energy of relaxation A, which is suitable for the activation energy of the polaron hopping, that is, charge carriers trapped at the oxygen vacancies.[50] The dielectric relaxation B originates from the interfacial polarization, such as grain boundaries, which is called MW polarization.[51] The discrepancy in E_B arises from the slight contribution of the IBLC effect to the dielectric response caused by the B-site disorder in $CaCu_3Fe_2Ta_2O_{12}$. $CaCu_3Ti_4O_{12}$ with giant dielectric response originates from semiconducting grains and insulating grain boundaries.[38] In contrast, it is hard to form semiconducting grains and insulating grain boundaries in $CaCu_3Fe_2Ta_2O_{12}$ due to the prominent electrical conductivity caused by the B-site disorder. Therefore, the IBLC effect slightly contributes to the dielectric response in $CaCu_3Fe_2Ta_2O_{12}$, which is consistent with the observed dielectric permittivity from Figure 5. Note that favorable agreement between experimental and fitting data over a wide frequency range for ε_r' strongly supports our model.

■ CONCLUSIONS

A new A-site-ordered oxide semiconductor, $CaCu_3Fe_2Ta_2O_{12}$, was prepared through a high-temperature combined with high-pressure approach. Combining the SXRD, NPD and TEM data, we reveal that the compound possesses an $Im\overline{3}$ space group, where it crystallizes to an A-site-ordered but B-site partial ordered quadruple perovskite structure. The introduction of the Jahn−Teller Cu^{2+} spin into the A site leads to spin ordering below 150 K. An antiferromagnetic ordering originates from the B-site Fe^{3+} sublattice and a ferromagnetic ordering arises from the A′-site Cu^{2+} sublattice. Interestingly, dielectric spectroscopy reveals two different relaxation behaviors. The low-temperature relaxation is dominated by a Debye-like relaxation, which is attributed to the charged carrier trapped among the oxygen vacancies, while the high-temperature relaxation arises from the MW polarization mechanism. These findings offer opportunities to design new perovskite oxides with attractive magnetic and dielectric properties.

■ ASSOCIATED CONTENT

Supporting Information

The Supporting Information is available free of charge at https://pubs.acs.org/doi/10.1021/acs.inorgchem.0c03229.

> UV−vis diffuse reflectance spectrum, plots of $(\alpha h\nu)^2$ versus energy $(h\nu)$, and band gap of $CaCu_3Fe_2Ta_2O_{12}$; temperature-dependent resistance, electrical resistivity, electrical conductivity, and conduction activation energy of $CaCu_3Fe_2Ta_2O_{12}$ (PDF)

■ AUTHOR INFORMATION

Corresponding Authors

Guobao Li − *College of Chemistry and Molecular Engineering, Peking University, Beijing 100871, P. R. China;* orcid.org/0000-0003-3061-193X; Email: liguobao@pku.edu.cn

Laijun Liu − *Guangxi Key Laboratory of Optical and Electronic Materials and Devices, Guilin University of Technology, Guilin 541004, China; Institute for Applied Materials - Energy Storage Systems (IAM - ESS), Karlsruhe Institute of Technology (KIT), 76344 Eggenstein-Leopoldshafen, Germany;* orcid.org/0000-0002-6889-2506; Email: ljliu2@163.com

Authors

Jianming Deng − *School of Aerospace Engineering, Beijing Institute of Technology, Beijing 100081, China*

Feifei Han − *Guangxi Key Laboratory of Optical and Electronic Materials and Devices, Guilin University of Technology, Guilin 541004, China*

Björn Schwarz − *Institute for Applied Materials - Energy Storage Systems (IAM - ESS), Karlsruhe Institute of Technology (KIT), 76344 Eggenstein-Leopoldshafen, Germany;* orcid.org/0000-0002-9461-1448

Michael Knapp − *Institute for Applied Materials - Energy Storage Systems (IAM - ESS), Karlsruhe Institute of Technology (KIT), 76344 Eggenstein-Leopoldshafen, Germany*

Helmut Ehrenberg − *Institute for Applied Materials - Energy Storage Systems (IAM - ESS), Karlsruhe Institute of Technology (KIT), 76344 Eggenstein-Leopoldshafen, Germany*

Weibo Hua − *Institute for Applied Materials - Energy Storage Systems (IAM - ESS), Karlsruhe Institute of Technology (KIT), 76344 Eggenstein-Leopoldshafen, Germany;* orcid.org/0000-0001-5372-4422

Manuel Hinterstein − *Institute for Applied Materials - Ceramic Materials and Technologies, Karlsruhe Institute of Technology, 76131 Karlsruhe, Germany*

Yun He − *Department of Physics, Guangxi Normal University, Guilin 541004, PR China*

Jie Wang − *Key Laboratory for RF Circuits and Systems, Ministry of Education, Key Laboratory of Large Scale Integrated Design of Zhejiang, Hangzhou Dianzi University, Hangzhou 310018, China*

Yuan Yuan − *Technology Development Center, Guilin Guiye Machinery Co., Ltd., Guilin 541119, China*

Complete contact information is available at:
https://pubs.acs.org/10.1021/acs.inorgchem.0c03229

Author Contributions

G.L. and L.L. designed and supervised the experiments. J.D., L.L., and Y.Y. prepared the sample. J.D. and F.H. performed dielectric properties, HRTEM, SAED, UV−vis diffuse reflectance spectrum, and electrical conductivity experiments. B.S. carried out magnetic property characterization. M.K., H.E., and M.H. performed SXRD and NPD experiments. Y.H. carried out the Mössbauer spectrum characterization. W.H. and W.J. proposed the fruitful suggestion on the manuscript. J.D. and F.H. wrote the manuscript. All authors discussed and contributed to the manuscript.

Notes

The authors declare no competing financial interest.

■ ACKNOWLEDGMENTS

We would like to acknowledge the support from the fellowship of the Helmholtz Association and the Karlsruhe Institute of Technology (KIT) and the Reunion Grant for Research Alumni of KIT. This work is also supported by the beamtime allocation at MSPD of the ALBA synchrotron (Barcelona, Spain) and SPODI at FRM II (Garching, Germany). The authors acknowledge the kind support for the academic research by Natural Science Foundation of Guangxi (FA198015, GA245006, BA245069, FA198015, and BA297029). L.L. thanks support from the High Level Innovation Team and Outstanding Scholar Program of Guangxi Institutes, the open Research Program of the Key Laboratory of RF Circuit and System, Ministry of Education, and the Key Laboratory of Large Scale Integrated Design of Zhejiang Province..

■ REFERENCES

(1) Rooksby, H. P. Compounds of the structural type of calcium titanate. *Nature* **1945**, *155*, 484−484.

(2) Long, Y. W.; Hayashi, N.; Saito, T.; Azuma, M.; Muranaka, S.; Shimakawa, Y. Temperature-induced A-B intersite charge transfer in an A-site-ordered $LaCu_3Fe_4O_{12}$ perovskite. *Nature* **2009**, *458*, 60−63.

(3) Shimakawa, Y. A-site-ordered perovskites with intriguing physical properties. *Inorg. Chem.* **2008**, *47*, 8562−8570.

(4) Larregola, S. A.; Zhou, J.; Alonso, J. A.; Pomjakushin, V.; Goodenough, J. B. New Routes to Synthesizing an Ordered Perovskite $CaCu_3Fe_2Sb_2O_{12}$ and Its Magnetic Structure by Neutron Powder Diffraction. *Inorg. Chem.* **2014**, *53*, 4281−4283.

(5) Yamada, I.; Ishiwata, S.; Terasaki, I.; Azuma, M.; Shimakawa, Y.; Takano, M. Synthesis, Structure, and Physical Properties of A-site Ordered Perovskites $ACu_3Co_4O_{12}$ (A = Ca and Y). *Chem. Mater.* **2010**, *22*, 5328−5332.

(6) Deng, J.; Liu, L.; Sun, X.; Liu, S.; Yan, T.; Fang, L.; Elouadi, B. Dielectric relaxation behavior and mechanism of $Y_{2/3}Cu_3Ti_4O_{12}$ ceramic. *Mater. Res. Bull.* **2017**, *88*, 320−329.

(7) Zeng, Z.; Greenblatt, M.; Subramanian, M. A.; Croft, M. Large low-field magnetoresistance in perovskite-type $CaCu_3Mn_4O_{12}$ without double exchange. *Phys. Rev. Lett.* **1999**, *82*, 3164.

(8) Shiraki, H.; Saito, T.; Yamada, T.; Tsujimoto, M.; Azuma, M.; Kurata, H.; Isoda, S.; Takano, M.; Shimakawa, Y. Ferromagnetic cuprates $CaCu_3Ge_4O_{12}$ and $CaCu_3Sn_4O_{12}$ with A-site ordered perovskite structure. *Phys. Rev. B* **2007**, *76*, 140403.

(9) Kobayashi, W.; Terasaki, I.; Takeya, J.; Tsukada, I.; Ando, Y. A novel heavy-fermion state in $CaCu_3Ru_4O_{12}$. *J. Phys. Soc. Jpn.* **2004**, *73*, 2373−2376.

(10) Yamada, I.; Takata, K.; Hayashi, N.; Shinohara, S.; Azuma, M.; Mori, S.; Muranaka, S.; Shimakawa, Y.; Takano, M. A Perovskite Containing Quadrivalent Iron as a Charge-Disproportionated Ferrimagnet. *Angew. Chem., Int. Ed.* **2008**, *47*, 7032−7035.

(11) Homes, C. C.; Vogt, T.; Shapiro, S. M.; Wakimoto, S.; Ramirez, A. P. Optical response of high-dielectric-constant perovskite-related oxide. *Science* **2001**, *293*, 673−676.

(12) Mu, C.-H.; Liu, P.; He, Y.; Zhou, J.-P.; Zhang, H.-W. An effective method to decrease dielectric loss of $CaCu_3Ti_4O_{12}$ ceramics. *J. Alloys Compd.* **2009**, *471*, 137−141.

(13) West, A. R.; Adams, T. B.; Morrison, F. D.; Sinclair, D. C. Novel high capacitance materials: -$BaTiO_3$: La and $CaCu_3Ti_4O_{12}$. *J. Eur. Ceram. Soc.* **2004**, *24*, 1439−1448.

(14) Liu, L.; Fan, H.; Fang, P.; Chen, X. Sol-gel derived $CaCu_3Ti_4O_{12}$ ceramics: Synthesis, characterization and electrical properties. *Mater. Res. Bull.* **2008**, *43*, 1800−1807.

(15) Sinclair, D. C.; Adams, T. B.; Morrison, F. D.; West, A. R. $CaCu_3Ti_4O_{12}$: one-step internal barrier layer capacitor. *Appl. Phys. Lett.* **2002**, *80*, 2153−2155.

(16) Fang, L.; Shen, M.; Zheng, F.; Li, Z.; Yang, J. Dielectric responses and multirelaxation behaviors of pure and doped $CaCu_3Ti_4O_{12}$ ceramics. *J. Appl. Phys.* **2008**, *104*, No. 064110.

(17) Burton, B. P.; Cockayne, E. Why Pb(B, B′)O_3 perovskites disorder at lower temperatures than Ba(B, B′)O_3 perovskites. *Phys. Rev. B* **1999**, *60*, R12542−R12545.

(18) Fauth, F.; Peral, I.; Popescu, C.; Knapp, M. The new material science powder diffraction beamline at ALBA synchrotron. *Powder Diffr.* **2013**, *28*, S360−S370.

(19) Hoelzel, M.; Senyshyn, A.; Juenke, N.; Boysen, H.; Schmahl, W.; Fuess, H. High-resolution neutron powder diffractometer SPODI at research reactor FRM II. *Nucl. Instrum. Methods Phys. Res., Sect. A* **2012**, *667*, 32−37.

(20) Rodriguez-Carvajal, J. *Satellite Meeting on Powder Diffraction of the XV IUCr*; 1990; Paper No. 127.

(21) Lufaso, M. W.; Barnes, P. W.; Woodward, P. M. Structure prediction of ordered and disordered multiple octahedral cation perovskites using SPuDS. *Acta Crystallogr., Sect. B: Struct. Sci.* **2006**, *62*, 397−410.

(22) Senn, M. S.; Chen, W.-t.; Saito, T.; García-Martín, S.; Attfield, J. P.; Shimakawa, Y. B-Cation Order Control of Magnetism in the 1322 Perovskite $CaCu_3Fe_2Nb_2O_{12}$. *Chem. Mater.* **2014**, *26*, 4832−4837.

(23) Patterson, A. L. The Scherrer formula for X-ray particle size determination. *Phys. Rev.* **1939**, *56*, 978.

(24) Brown, I. D.; Altermatt, D. Bond-valence parameters obtained from a systematic analysis of the inorganic crystal structure database. *Acta Crystallogr., Sect. B: Struct, Sci., Cryst. Eng. Mater.* **1985**, *41*, 244−247.

(25) Lufaso, M. W.; Woodward, P. M. Prediction of the crystal structures of perovskites using the software program SPuDS. *Acta Crystallogr., Sect. B: Struct. Sci.* **2001**, *57*, 725−738.

(26) Shannon, R. D. Revised effective ionic radii and systematic studies of inter-atomic distances in halides and chalcogenides. *Acta Crystallogr., Sect. A: Found. Adv.* **1976**, *32*, 751−767.

(27) Gibb, T. C. Study of magnetic relaxation in the perovskite $SrLaFeSnO_6$ by M̈ssbauer spectroscopy. *J. Mater. Chem.* **1992**, *2*, 415−422.

(28) Battle, P. D.; Gibb, T. C.; Herod, A. J.; Kim, S.-H.; Munns, P. H. Investigation of magnetic frustration in A_2FeMO_6 (A = Ca, Sr, Ba; M = Nb, Ta, Sb) by magnetometry and m̈ssbauer spectroscopy. *J. Mater. Chem.* **1995**, *5*, 865−870.

(29) Mizumaki, M.; Saito, T.; Shiraki, H.; Shimakawa, Y. Orbital Hybridization and Magnetic Coupling of the A-Site Cu Spins in $CaCu_3B_4O_{12}$ (B = Ti, Ge, and Sn) Perovskites. *Inorg. Chem.* **2009**, *48*, 3499−3501.

(30) Shimakawa, Y.; Saito, T. A-site magnetism in A-site-ordered perovskite-structure oxides. *Phys. Status Solidi B* **2012**, *249*, 423−434.

(31) Dass, R. I.; Goodenough, J. B. Multiple magnetic phases of $La_2CoMnO_{6-\delta}$(0 <~δ <~0.05). *Phys. Rev. B: Condens. Matter* **2003**, *67*, No. 014401.

(32) Rearick, T. M.; Catchen, G. L.; Adams, J. M. Combined magnetic-dipole and electric-quadrupole hyperfine interactions in rare-earth orthoferrite ceramics. *Phys. Rev. B* **1993**, *48*, 224.

(33) Li, H.; Zhu, Z.; Ge, Z.; Sun, A.; Tian, Y. Ferrimagnetic semiconductor with a direct bandgap. *Appl. Phys. Lett.* **2020**, *116*, 122401.

(34) Pirovano, A.; Lacaita, A. L.; Benvenuti, A.; Pellizzer, F.; Bez, R. Electronic switching in phase-change memories. *IEEE Trans. Electron Devices* **2004**, *51*, 452−459.

(35) Ni, L.; Chen, X. M. Enhancement of Giant Dielectric Response in $CaCu_3Ti_4O_{12}$ Ceramics by Zn Substitution. *J. Am. Ceram. Soc.* **2010**, *93*, 184−189.

(36) Ni, L.; Chen, X. M.; Liu, X. Q. Structure and modified giant dielectric response in $CaCu_3(Ti_{1-x}Sn_x)_4O_{12}$ ceramics. *Mater. Chem. Phys.* **2010**, *124*, 982−986.

(37) Thongbai, P.; Putasaeng, B.; Yamwong, T.; Amornkitbamrung, V.; Maensiri, S. Liquid phase sintering behavior and improvement of giant dielectric properties by modifying microstructure and electrical response at grain boundaries of $CaCu_3Ti_{4-x}Mo_xO_{12}$ ceramics. *J. Alloys Compd.* **2014**, *582*, 747−753.

(38) Liu, L.; Ren, S.; Liu, J.; Han, F.; Zhang, J.; Peng, B.; Wang, D.; Bokov, A. A.; Ye, Z.-G. Localized polarons and conductive charge carriers: Understanding $CaCu_3T_{i4}O_{12}$ over a broad temperature range. *Phys. Rev. B* **2019**, *99*, No. 094110.

(39) Liu, L.; Shi, D.; Zheng, S.; Huang, Y.; Wu, S.; Li, Y.; Fang, L.; Hu, C. Polaron relaxation and non-ohmic behavior in $CaCu_3Ti_4O_{12}$ ceramics with different cooling methods. *Mater. Chem. Phys.* **2013**, *139*, 844−850.

(40) Chen, W.-t.; Mizumaki, M.; Seki, H.; Senn, M. S.; Saito, T.; Kan, D.; Attfield, J. P.; Shimakawa, Y. A half-metallic A-and B-site-ordered quadruple perovskite oxide $CaCu_3Fe_2Re_2O_{12}$ with large magnetization and a high transition temperature. *Nat. Commun.* **2014**, *5*, 3909.

(41) Chen, W.-t.; Mizumaki, M.; Saito, T.; Shimakawa, Y. Frustration relieved ferrimagnetism in novel A-and B-site-ordered quadruple perovskite. *Dalton Trans.* **2013**, *42*, 10116−10120.

(42) Byeon, S.-H.; Lee, S.-S.; Parise, J. B.; Woodward, P. M.; Hur, N. H. New Ferrimagnetic Oxide $CaCu_3Cr_2Sb_2O_{12}$: High-Pressure Synthesis, Structure, and Magnetic Properties. *Chem. Mater.* **2005**, *17*, 3552−3557.

(43) Byeon, S.-H.; Lee, S.-S.; Parise, J. B.; Woodward, P. M. New Perovskite Oxide $CaCu_3Cr_2Ru_2O_{12}$: Comparison with Structural, Magnetic, and Transport Properties of the $CaCu_3B_2B'_2O_{12}$ Perovskite Family. *Chem. Mater.* **2006**, *18*, 3873−3877.

(44) Byeon, S.-H.; Lufaso, M. W.; Parise, J. B.; Woodward, P. M.; Hansen, T. High-Pressure Synthesis and Characterization of Perovskites with Simultaneous Ordering of Both the A- and B-Site Cations, $CaCu_3Ga_2M_2O_{12}$ (M = Sb, Ta). *Chem. Mater.* **2003**, *15*, 3798−3804.

(45) Gerhardt, R. Impedance and dielectric spectroscopy revisited: distinguishing localized relaxation from long-range conductivity. *J. Phys. Chem. Solids* **1994**, *55*, 1491−1506.

(46) Mai, C.; Etienne, S.; Perez, J.; Johari, G. P. Modulus and internal friction in phosphate-silicate bioactive glass. *J. Non-Cryst. Solids* **1985**, *74*, 119−127.

(47) Raevski, I. P.; Maksimov, S. M.; Fisenko, A. V.; Prosandeyev, S. A.; Osipenko, I. A.; Tarasenko, P. F. Study of intrinsic point defects in oxides of the perovskite family: II. Experiment. *J. Phys.: Condens. Matter* **1998**, *10*, 8015.

(48) Morrison, F. D.; Sinclair, D. C.; West, A. R. Characterization of lanthanum-doped barium titanate ceramics using impedance spectroscopy. *J. Am. Ceram. Soc.* **2001**, *84*, 531.

(49) Batra, A. K.; Currie, J. R.; Alim, M. A.; Aggarwal, M. D. Impedance response of polycrystalline tungsten oxide. *J. Phys. Chem. Solids* **2009**, *70*, 1142−1145.

(50) Hu, W.; Liu, Y.; Withers, R. L.; Frankcombe, T. J.; Norén, L.; Snashall, A.; Kitchin, M.; Smith, P.; Gong, B.; Chen, H.; Schiemer, J.; Brink, F.; Wong-Leung, J. Electron-pinned defect-dipoles for high-performance colossal permittivity materials. *Nat. Mater.* **2013**, *12*, 821−826.

(51) Song, Y.; Wang, X.; Zhang, X.; Sui, Y.; Zhang, Y.; Liu, Z.; Lv, Z.; Wang, Y.; Xu, P.; Song, B. The contribution of doped-Al on the colossal permittivity properties of $Al_xNb_{0.03}Ti_{0.97-x}O_2$ rutile ceramics. *J. Mater. Chem. C* **2016**, *4*, 6798−6805.